ACS Catalysis

pubs.acs.org/acscatalysis Research Article

Structural and Catalytic Properties of Isolated Pt^{2+} Sites in Platinum Phosphide (PtP_2)

Jiajing Kou, Johnny Zhu Chen, Junxian Gao, Xiaoben Zhang, Jie Zhu, Arnab Ghosh, Wei Liu, A. Jeremy Kropf, Dmitry Zemlyanov, Rui Ma, Xinwen Guo, Abhaya K. Datye, Guanghui Zhang,* Liejin Guo,* and Jeffrey T. Miller*

Cite This: *ACS Catal.* 2021, 11, 13496−13509 Read Online

ACCESS | Metrics & More | Article Recommendations | Supporting Information

ABSTRACT: This article describes the synthesis and catalytic properties of supported, 2−3 nm platinum phosphide (PtP_2) nanoparticles (NPs). Depending on the P loading, two PtP_2 structures are formed, that is, a PtP_2 surface on a (metallic) Pt core (Pt@PtP_2) and single-phase PtP_2 NPs. The structures were determined using extended X-ray absorption fine structure , in situ synchrotron X-ray diffraction, and scanning transmission electron microscopy. In PtP_2 NPs, Pt^{2+} ions are geometrically isolated by P_2^{2-} ions, at a Pt−Pt distance of 4.02 Å, which is much longer than 2.78 Å in (metallic) Pt NPs. The oxidation state of Pt in PtP_2 NPs was determined by in situ X-ray absorption near-edge structure and in situ X-ray photoelectron spectroscopy and was found to be consistent with Pt^{2+} ions even after treatment in H_2 at 550 °C. Unlike Pt NPs, which are highly active for propylene hydrogenation at room temperature, PtP_2 NPs are not active below about 150 °C, suggesting the absence of metallic surface Pt. In contrast to metallic Pt, which is poorly selective for acetylene hydrogenation, PtP_2 NPs display high selectivity toward ethylene. PtP_2, also has high olefin selectivity for propane dehydrogenation, although the rate per g Pt is about 7 times lower than that of metallic Pt NPs of the same size. In situ resonant inelastic X-ray scattering spectroscopy shows that the energy of the filled Pt 5d valence orbitals is 1.5 eV lower than that of metallic Pt, which leads to weaker adsorbate binding consistent with its catalytic properties. A H_2-stable Pt^{2+} site suggests different catalytic applications for these catalysts as compared to Pt NPs.

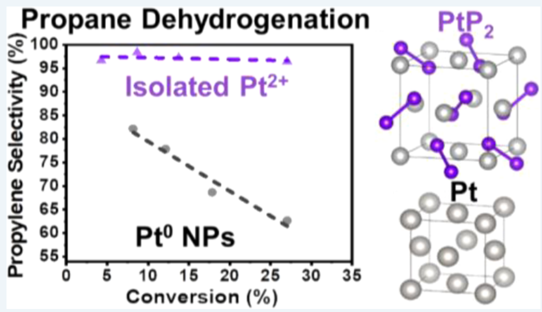

KEYWORDS: *isolated Pt^{2+} catalytic site, PtP_2 nanoparticle, propane dehydrogenation, in situ X-ray absorption spectroscopy, in situ resonant inelastic X-ray scattering*

1. INTRODUCTION

The majority of commercial processes for production of petrochemicals and fuels utilize heterogeneous catalysts, and platinum is one of the most versatile active metals for many reactions. Pt is highly effective for both oxidation and reduction reactions, and for the majority of these applications, metallic Pt is the active form of the catalyst. In addition, bimetallic alloys[1−10] are generally more selective and stable and have been widely studied for hydrogenation/dehydrogenation,[3,11] naphtha reforming,[3,12,13] water gas shift reaction,[14,15] biomass reforming,[16] auto-exhaust emission control, CO and hydrocarbon oxidation,[17,18] electrocatalytic transformation,[19−21] etc. For example, Pt−Sn bimetallic catalysts have been widely studied and used as industrial catalysts for propane dehydrogenation to propylene.[22,23] The incorporated Sn atoms dilute large Pt ensembles, which effectively inhibits side reactions such as hydrogenolysis and coke formation. In addition, Sn modifies the energy of the Pt 5d orbitals, which weakens the metal−adsorbate bond energies. However, Pt-based bimetallic catalysts still suffer from coking and sintering and require carbon-burning and Cl_2-regenerative treatments, while phase segregation and separation occasionally occurs, causing irreversible deactivation of bimetallic catalysts.[24−26] Because of their industrial and fundamental importance, the development of new catalytic materials with new properties and potentially new reactions remains an active research field.

Metal phosphides can usually be understood as P-doped metal "alloys", and the bond formation of metal and P atoms can greatly modify the geometric and electronic structures of metal atoms, similar to bimetallic alloys.[27−29] However, compared with bimetallic alloys, the smaller size and higher electronegativity of P atoms offer additional flexibility for obtaining desired properties, which provides a feasible strategy for robust catalyst design.[30,31] Metal-rich phosphides, for

Received: August 31, 2021
Revised: October 7, 2021
Published: October 22, 2021

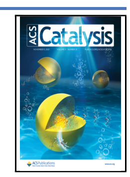

https://doi.org/10.1021/acscatal.1c03970
ACS Catal. 2021, 11, 13496−13509

example, M_3P, M_2P, and MP, with structures containing metal−metal bonds, display metallic properties for a number of heterogeneous catalytic applications[32] including electrochemistry[33] for hydrogen evolution,[34,35] hydroprocessing for the removal of S, N, and O from petroleum,[27,36−40] olefin hydroformylation,[41] alkane dehydrogenation,[42−44] and so forth. Transition-metal phosphides often have high thermal stability, which suggests that these might be potential catalysts for high-temperature reactions.[43−46] For example, Ni_2P has higher olefin selectivity than Ni nanoparticles (NPs) for propane dehydrogenation at 550 °C. The improved olefin selectivity was suggested to be due to weaker olefin adsorption and better coke resistance.[43,44] A more metal-rich phase, $Ni_{15}P_2$, however, led to increased deactivation.[44] Similar findings were found for Ru phosphide catalysts. RuP nanocrystal catalysts displayed high olefin selectivity and better stability for propane dehydrogenation than Ru_2P.[47] In contrast with Ni, Fe, and Ru NPs, which convert alkanes to methane and coke with little selectivity to olefins, metal phosphides with a proper structure can have the high activity of Group 8 metal NPs but with high catalytic selectivity and improved stability. The thermal stability and excellent catalytic performance of Ni_2P and RuP compared to those of pure metal NPs suggest that Pt phosphide (PtP_2) might also be an effective hydrogenation/dehydrogenation catalyst.

In this work, we report a series of supported, 2−3 nm PtP_2 catalysts with non-metallic character. The PtP_2 catalyst structures were determined using in situ X-ray absorption spectroscopy (XAS), in situ synchrotron X-ray diffraction (sXRD), and scanning transmission electron microscopy (STEM). The oxidation state of Pt in the PtP_2 catalysts was determined to be Pt^{2+} using X-ray absorption near-edge structure (XANES) and X-ray photoelectron spectroscopy (XPS). Thus, the catalytic site in PtP_2 NPs is an isolated Pt^{2+} ion on the NP surface. In situ resonant inelastic X-ray scattering (RIXS) was used to determine the effect of P_2^{2-} ions on the energy of the Pt 5d valence orbitals as compared to monometallic Pt NPs. The structural and electronic changes provide a fundamental understanding of the role of P in the catalytic performance. Propane dehydrogenation, propylene hydrogenation, and selective acetylene hydrogenation were performed to evaluate the catalytic properties. Unlike metallic Pt NPs, PtP_2 does not chemisorb CO or hydrogenate olefins at room temperature (RT). PtP_2 catalysts display high olefin selectivity for propane dehydrogenation with rates approaching those of metallic Pt NPs and significantly higher than those of other non-metallic, single-site dehydrogenation catalysts. PtP_2 shows significantly higher ethylene selectivity for acetylene hydrogenation than Pt NPs. These results demonstrate that the different catalytic properties of isolated Pt^{2+} catalytic sites endow them with potential for exhibiting a better performance than Pt NPs for some reactions, especially those in which single-site ions are the preferred active sites.

2. EXPERIMENTAL SECTION

2.1. Catalyst Synthesis. All catalysts were synthesized by sequential incipient wetness impregnation (IWI). To prepare Pt/SiO_2 with a target Pt loading of 2 wt %, 0.2 g of tetraamine platinum nitrate [$Pt(NH_3)_4(NO_3)_2$, 99.995%] was dissolved in 2.75 mL deionized water, and concentrated NH_4OH was added to obtain a clear solution with pH around 11. This solution was added dropwise to 5.0 g silica gel (SiO_2, 480 m^2/g, 0.75 mL/g pore volume, 99%) with continuous mixing. The obtained sample was dried at RT for 3 h before drying at 105 °C overnight and then calcined at 225 °C for 3 h. The reduction step of Pt/SiO_2 was performed under 5% H_2/N_2 at 225 °C for 30 min, then at 250 °C for 30 min, followed by 550 °C for another 30 min.

To prepare Pt−P catalysts, Pt/SiO_2 was first obtained by the above method but not reduced. The amount of phosphoric acid [H_3PO_4, 85% aq] based on the P/Pt molar ratios of 10:1, 20:1, and 50:1 was dropwise added to the unreduced Pt/SiO_2. The obtained solid was dried at RT for 3 h before drying in an oven at 105 °C overnight and then calcined at 600 °C for 1 h. The Pt−P samples were finally reduced at 550 °C under 5% H_2/N_2. The obtained catalyst was denoted as Pt-P-*x*, where *x* denotes the molar ratio of P/Pt. Pt-P-10, Pt-P-20, and Pt-P-50 were synthesized using this method. For comparison, a P/SiO_2 sample was prepared using the same method and with the same P loading as that of the Pt-P-50 sample.

2.2. Characterizations. *2.2.1. Scanning Transmission Electron Microscopy.* The atomic resolution microscopy analysis of Pt−P catalysts was performed on a JEM ARM200F thermal-field emission microscope with a probe Cs-corrector working at 200 kV, which is located at the Center for Electron Microscopy of Dalian Institute of Chemical Physics (DICP), Chinese Academy of Sciences. In the high-angle annular dark-field (HAADF) imaging, a convergence angle of ∼23 mrad and a collection angle range of 68−174 mrad were adapted for the incoherent atomic number imaging.

Additionally, the Titan Themis G3 environmental transmission electron microscope (Thermo Scientific Company) operated at 300 kV in the TEM mode was utilized as complementary to the ARM200F microscope for imaging the Pt-P-50 catalyst. For all the STEM/TEM sample preparation, catalysts were dispersed in ethanol and dropped onto copper grids and dried on a hot plate (150 °C). Several images were taken from randomly selected locations on the catalysts to analyze the size distribution based on over 400 NPs.

2.2.2. In Situ XAS. In situ XAS measurements at the Pt L_3 edge (11.564 keV) in transmission mode were performed at the 10-BM-B beamline at the Advanced Photon Source (APS), Argonne National Laboratory. Catalysts and reference compounds were ground into fine powders and pressed into a sample holder containing six wells. Then, the holder was loaded into a quartz tube allowing gas flow so that samples could be treated prior to measurements. The catalysts were treated with 3.5% H_2/He at 550 °C and then cooled to RT in flowing He before moving to the beamline to acquire data. For internal energy calibration, a Pt foil scan was simultaneously obtained. Athena software was used to calibrate energy and normalize the data, and the edge energy was determined by the first maximum peak in the first derivative of the XANES spectra.[48] Extended X-ray absorption fine structure (EXAFS) spectra were fit using a least-squares fit in *R*-space of k^2-weighted Fourier transform (FT) to determine the coordination number (CN) and bond distances (*R*) between Pt and its neighbors using the Artemis software,[48] and the *k* range for FT of the Pt L_3 edge was Δk = 2.75 − 12.0 $Å^{-1}$. The S_0^2 value was determined from fitting the Pt foil standard. The σ^2 values were determined from the k^2-weighted EXAFS of the inverse FT of the isolated first shell in *k*-space for each catalyst.

2.2.3. X-ray Photoelectron Spectroscopy. XPS measurement was performed using a Kratos AXIS Ultra DLD Imaging spectrometer, using monochromatic Al Kα radiation as an excitation source. Prior to spectral acquisition, fresh catalysts

https://doi.org/10.1021/acscatal.1c03970
ACS Catal. 2021, 11, 13496−13509

were reduced in a catalyst cell by 5% H_2 balanced with Ar at 550 °C for 1 h, and then transferred under ultrahigh vacuum into the analysis chamber without exposure to air. The data were analyzed with CasaXPS software. For charge correction, the C 1s peak of the adventitious carbon was set to a binding energy of 284.8 eV. The Shirley type background was substracted and curve-fitting was performed using the synthetic function of Lorentzian blended with Gaussian.

2.2.4. In Situ sXRD. In situ sXRD measurements were performed at the 11-ID-C beamline at the APS, Argonne National Laboratory. The data were collected in the transmission mode using a PerkinElmer large-area detector and using X-rays of $\lambda = 0.1173$ Å at 105.091 keV calibrated by fitting the diffraction pattern of the CeO_2 reference. Samples were pressed into thin wafers, then loaded into a Linkam Scientific TS1500 heating stage equipped with water cooling. Prior to measurements, the stage was purged with He for 5 min at RT and then ramped to 550 °C in 3.5% H_2/He at 50 mL/min. Diffraction patterns were acquired after reduction at 550 °C for 20 min, and also collected at 35 °C after being cooled down in the same atmosphere. The 2-D scattering images were integrated to 1-D intensity versus 2θ plots by using Fit2D software.[49] Materials Analysis Using Diffraction (MAUD) software was used to simulate standard diffraction patterns of Pt face-centered cubic (fcc) and PtP_2 phases, which were used to determine the crystal structure of Pt−P catalysts in comparison with experimental diffraction patterns.[50]

2.2.5. In Situ RIXS. RIXS measurements were performed at the MR-CAT 10-ID beamline at the APS, Argonne National Lab. Samples were pressed into self-supporting wafers and were placed at a 45° angle with respect to the incident beam. The small reactor with internal resistively heated plates has been previously described.[51] Samples were reduced at 550 °C in 3% H_2/He at 50 mL/min for 20 min and then cooled to 200 °C for measurement.

A spectrometer based on the Laue geometry was used for RIXS measurements and has been described previously.[5] The cylindrically bent silicon analyzer crystal had the following properties: $\rho = 350$ mm, a thickness of 55 μm, [100] wafer normal, and $\langle 133 \rangle$ reflection. The entire emission spectrum was collected at each incident energy; both the analyzer and detector positions were fixed during measurements.

2.2.6. In Situ Infrared Spectroscopy. In situ diffuse reflectance infrared FT (DRIFT) spectra were collected on a Nicolet iS50 spectrometer with a mercury cadmium telluride detector cooled by liquid nitrogen. Prior to the test, ~20 mg of the sample was reduced at 550 °C under 5% H_2 for 30 min, and the background spectrum was collected after purging with N_2 at RT for 40 min. Then, the prereduced samples were exposed to 10 vol % CO in N_2 at 25 °C for 40 min, and the sample IR spectra were collected after purging with N_2 for 40 min.

2.3. Catalytic Evaluation. *2.3.1. Propylene Hydrogenation and Propane Dehydrogenation.* Propylene hydrogenation and propane dehydrogenation were carried out on a quartz fixed-bed reactor with a quartz tube of 3/8 in. OD. To vary the initial conversion, the loaded catalysts ranging from 10 to 300 mg were diluted with SiO_2 to 1.0 g. A thermocouple was placed at the center of the catalyst bed to measure the reaction temperature. Before each test, the catalyst was reduced for 30 min at 550 °C with 100 mL/min 5% H_2/N_2. The flow of 5% C_3H_8 and 5% H_2 was adjusted to vary the initial conversion for PDH at a reaction temperature of 550 °C. The gas products were analyzed with an Agilent 7890A gas chromatograph system equipped with a flame ionization detector. In PDH, five kinds of light hydrocarbons were detected: CH_4, C_2H_6, C_2H_4, C_3H_8, and C_3H_6. The propane conversion and propylene selectivity were calculated using eqs 1 and 2. The rate of reaction was calculated using eq 3. A first-order deactivation model was used to estimate the rate of catalyst deactivation, and the deactivation coefficient (k_d) was determined as shown in eq 4, where $Conv_0$ is defined as the initial conversion and $Conv_t$ is the conversion at time t.

$$\text{Conversion (\%)} = \frac{\text{moles of } C_3H_8 \text{ in inlet} - \text{moles of } C_3H_8 \text{ in outlet}}{\text{moles of } C_3H_8 \text{ in inlet}} \times 100\% \quad (1)$$

$$\text{Selectivity (\%)} = \frac{\text{moles of } C_3H_6}{\text{moles of } C_3H_6 + \frac{2 \times \text{moles of } C_2}{3} + \frac{\text{moles of } CH_4}{3}} \times 100\% \quad (2)$$

$$\text{Rate} = \frac{\text{molar flow rate of } C_3H_8 \times \text{conversion}}{\text{moles of Pt}} \quad (3)$$

$$k_d = \frac{\ln\left(\frac{1 - Conv_t}{Conv_t}\right) - \ln\left(\frac{1 - Conv_0}{Conv_0}\right)}{t} \quad (4)$$

2.3.2. Selective Acetylene Hydrogenation. Selective hydrogenation of acetylene was carried out in a 6 mm OD quartz tube with glass wool plugs on each side to retain the catalyst. Pt/SiO_2 and Pd/Al_2O_3 catalysts were used as reference catalysts, with 20 mg of catalyst diluted with an equal volume of SiC. Due to their lower reactivity, the Pt−P powders were tested with 180 mg of catalyst to achieve similar conversions of acetylene. A thermocouple was placed in the catalyst bed to measure the reaction temperature. Before each test, each catalyst was reduced for 60 min at 350 °C with 50 mL/min 4% H_2/N_2. The reactant gas was composed of 1% C_2H_2, 4% H_2 and the rest balanced with N_2 at a total flow rate of 50 mL/min. The acetylene conversion and ethylene selectivity were calculated as shown below

$$\text{acetylene conversion (\%)} = \frac{\text{moles of } C_2H_2 \text{ in inlet} - \text{moles of } C_2H_2 \text{ in outlet}}{\text{moles of } C_2H_2 \text{ in inlet}} \times 100\% \quad (5)$$

$$\text{ethylene selectivity (\%)} = \frac{\text{moles of } C_2H_4 \text{ in outlet}}{\text{moles of } C_2H_2 \text{ in inlet} - \text{moles of } C_2H_2 \text{ in outlet}} \times 100\% \quad (6)$$

3. RESULTS

3.1. Synthesis of Silica-Supported PtP_2 Catalysts. Transition-metal phosphides are most often synthesized as colloidal NPs using metal−organic precursor decomposition,[52] solvothermal,[53] and solid-phase reaction[54] methods. Typically, the NP sizes are larger than 5 nm, and often much larger,

https://doi.org/10.1021/acscatal.1c03970
ACS Catal. 2021, 11, 13496−13509

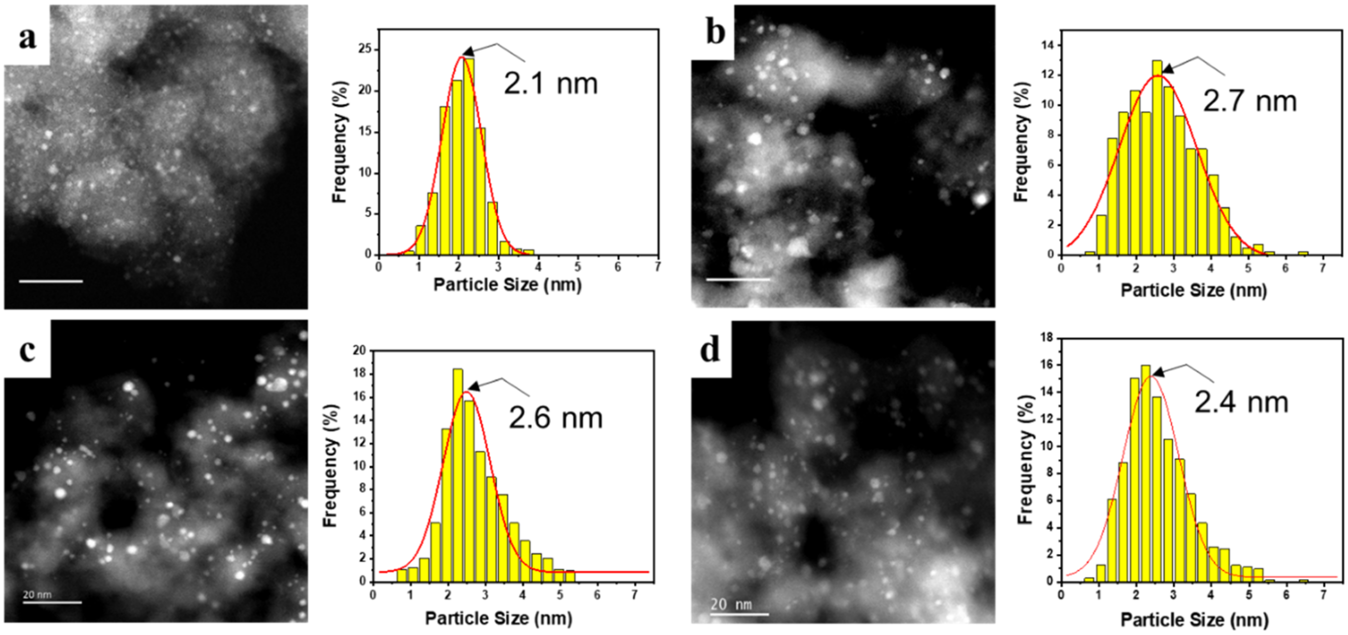

Figure 1. STEM images and particle size distributions for (a) Pt/SiO_2, (b) Pt-P-10, (c) Pt-P-20, and (d) Pt-P-50.

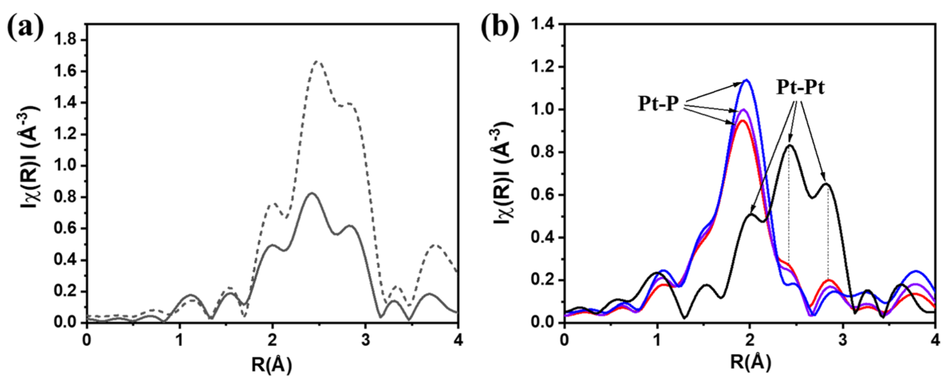

Figure 2. k^2-weighted magnitudes of the FT of EXAFS spectra at the Pt L_3 edge of (a) Pt foil (dash line) and Pt/SiO_2 (black line), (b) Pt/SiO_2 (black line), Pt-P-10 (red line), Pt-P-20 (purple line), and Pt-P-50 (blue line).

Table 1. Edge Energy and EXAFS Data at the Pt L_3 Edge for the Fully Reduced Supported Pt Catalysts

catalyst	edge energy (keV)	scattering path	R (Å)	CN	σ^2
Pt/SiO_2	11.5640	Pt−Pt	2.74 ± 0.02	8.4 ± 0.8	0.007 ± 0.001
Pt-P-10	11.5652	Pt−Pt	2.76 ± 0.01	2.4 ± 0.4	0.007 ± 0.001
		Pt−P	2.33 ± 0.02	3.5 ± 0.2	0.007 ± 0.001
Pt-P-20	11.5654	Pt−Pt	2.76 ± 0.01	1.8 ± 0.4	0.007 ± 0.001
		Pt−P	2.34 ± 0.01	3.7 ± 0.5	0.007 ± 0.001
Pt-P-50	11.5655	Pt−P	2.36 ± 0.01	4.4 ± 0.4	0.007 ± 0.001

which are not ideal for catalytic applications. In addition, the synthesis approaches are not easily reproduced for large scale applications. Here, PtP_2 are directly synthesized on a higher surface area oxide support. The synthesis approach is to first impregnate an aqueous solution of $Pt(NH_3)_4(NO_3)_2$ onto the silica surface in NH_4OH. The basic solution deprotonates the support hydroxyl groups leading to a negative surface charge. Under these impregnation conditions, the $Pt(NH_3)_4{}^{2+}$ ions are uniformly distributed.[55] After drying, aqueous solutions of phosphoric acid are added, dried, and heated in air to 600 °C. Because these catalysts will be used for hydrogenation reactions, they were additionally reduced at 550 °C. At these high temperatures, the metal salts reduce to form PtP_2. P to Pt molar ratios were from 1 to 50. For P to Pt ratios below about 4, the NPs were largely metallic Pt, while at ratios greater than about 10, predominantly PtP_2 was formed.

The particle sizes of these Pt−P catalysts as well as Pt/SiO_2 were determined by STEM. The uniform distribution of the bright spots suggests a narrow range of the particle sizes shown in Figure 1. The particle size distributions of all catalysts are similar ranging between 2 and 3 nm. For example, the average particle size of Pt/SiO_2 is 2.1 nm, and the average particle sizes of Pt-P-10, Pt-P-20, and Pt-P-50 are 2.7, 2.6, and 2.4 nm, respectively.

3.2. Geometric Structures of Pt and Pt−P NPs. The local Pt coordination was determined by XAS at the Pt L_3 edge

https://doi.org/10.1021/acscatal.1c03970
ACS Catal. 2021, 11, 13496−13509

(11.564 keV). Figure 2 shows the k^2-weighted magnitudes of the FT of the EXAFS spectra of Pt and Pt−P NPs. The magnitude and imaginary parts of the FT of the EXAFS at the Pt L_3 edge of all catalysts were fitted to determine the CN and bond distances (R), as shown in Figure S1 and Table 1. The spectrum of Pt/SiO_2 shows the same shape and peak position as that of a Pt foil (Figure 2a), where there are three main peaks between about 2 and 3 Å (phase uncorrected distance), indicating these samples were fully reduced. The Pt−Pt CN (CN_{Pt-Pt}) of Pt/SiO_2 was 8.1 at 2.74 Å, and a lower CN_{Pt-Pt} and a slightly shorter bond distance (2.74 Å) compared to those of the Pt foil (2.77 Å) are typical characteristics of NPs.[56]

For comparison, the k^2-weighted magnitudes of the FT of the EXAFS spectra of Pt and Pt−P NPs are shown in Figure 2b. The Pt-P-50 catalyst (blue spectrum) has a very different spectrum from that of Pt NPs (black spectrum). A large peak located around 2 Å indicates the presence of shorter bonds, but no peaks were observed in the region where Pt−Pt scattering is expected. The spectrum was fitted with a Pt−P scattering, from which a Pt−P CN (CN_{Pt-P}) of 4.4 at 2.36 Å was obtained.

Compared with Pt-P-50 and Pt NPs, the EXAFS spectra of Pt-P-10 and Pt-P-20 catalysts show a large peak at about 2 Å and much smaller peaks between 2 and 3 Å, suggesting the presence of Pt−P bonds and a small fraction of Pt−Pt bonds, respectively, as shown in Figures 2b and S2. Thus, two scattering pairs of Pt−Pt and Pt−P were used to fit the EXAFS of Pt-P-10 (Figure S1), resulting in a CN_{Pt-Pt} of 2.4 at 2.76 Å and a CN_{Pt-P} of 3.5 at 2.33 Å. A Pt−Pt bond distance of 2.76 Å is characteristic of metallic Pt. The small CN in these two samples suggests only minor amounts of metallic Pt. As the P loading increases, for example, Pt-P-20, the CN_{Pt-Pt} decreases slightly to 1.8 at 2.76 Å and the CN_{Pt-P} increases to 3.7 at 2.33 Å.

While XAS shows there are Pt−P bonds in these catalysts, X-ray absorption is a local scattering technique and does not provide information on the crystalline order of the NPs. Because of their small size, in situ sXRD was required to identify the phase. Due to the high X-ray energy (105.70 keV or λ = 0.1173 Å), the resulting diffraction patterns were obtained at lower 2θ angles than those from a laboratory diffractometer, typically from 0 to 10°, as shown in Figure 3. The high flux of the synchrotron X-ray beam also gives a better signal-to-noise ratio to characterize the NPs. In order to reduce the effects of thermal strain, the sXRD patterns for all the catalysts were obtained at RT in a H_2 atmosphere after reduction in H_2 at 550 °C. Figure 3 shows the reflections of Pt-P-10 match those of the simulated Pt fcc structure. Although XAS suggested two components in Pt-P-10, the sXRD pattern shows only metallic Pt NPs. It is likely that scattering from the small size and the weak scattering of the P atoms in the diffraction pattern of the PtP_2 regions could not be detected. For Pt-P-20, in addition to the characteristic peaks of Pt fcc, there are additional peaks in the sXRD pattern, which match with those of PtP_2 (ICSD 9015002). For Pt-P-50, there were large peaks due to the P species that dominated the diffraction pattern, as shown in Figure S3, thus the structure of the Pt−P phase could not be determined.

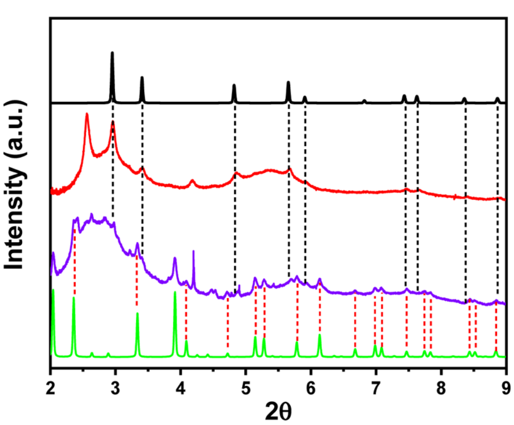

Figure 3. Synchrotron XRD patterns of Pt-P-10 (red line), Pt-P-20 (purple line), Pt simulation (black line, ICSD 9012957), and PtP_2 simulation (green line, ICSD 9015002).

To confirm the structure of the Pt-P-50 catalyst, HAADF STEM was conducted on Pt-P-50, and the image is shown in Figure 4. The atomic resolution STEM shows a highly ordered

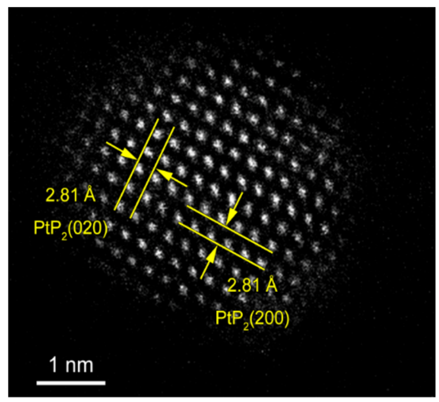

Figure 4. High-resolution STEM image of the Pt-P-50 catalyst.

NP with a zone axis ⟨001⟩ for Pt-P-50. The lattice spacing of 2.81 Å is ascribed to (020) and (200) planes of the PtP_2 structure. The image contrast confirms that Pt-P-50 shows a fully ordered PtP_2 structure in agreement with the EXAFS results.

In summary, Pt-P-50 has a fully ordered PtP_2 structure, as confirmed by STEM and EXAFS, whereas there are both Pt and PtP_2 domains within the NPs present in Pt-P-10 and Pt-P-20, as evident from EXAFS and XRD. To better understand the structures of the latter two catalysts, the surface composition of the NPs was determined by difference analysis of in situ XAS under reducing and mild oxidizing conditions.[4,6,57] The k^2-weighted magnitudes of the FT of EXAFS spectra of the reduced and oxidized Pt−P catalysts are shown in Figure 5. There is no change in these spectra between reduced (solid) and oxidized (dotted) for either PtP_2 structure (Figure 5b) or the Pt-P-20 catalyst (Figure 5a), which contains both PtP_2 and Pt. Similar results were obtained for Pt-P-10 (Figure S4). The XANES spectra of the Pt-P-50, Pt-P-20, and Pt-P-10 (Figure S5) also showed no change upon oxidation consistent with the EXAFS results.

Metallic Pt is oxidized in air at RT leading to the loss of Pt−Pt bonds and the formation of Pt−O bonds. The absence of Pt oxidation in Pt-P-10 and Pt-P-20 suggests that there is no metallic Pt surface but likely is PtP_2. Thus, the remaining Pt−Pt scattering observed by XAS and sXRD is from the NP core. In other words, Pt-P-10 and Pt-P-20 appear to be core−shell structures with a PtP_2 shell with a metallic Pt core. The core−shell structure is also confirmed by the catalytic performance, which will be shown later. The absence of exposed metallic Pt

https://doi.org/10.1021/acscatal.1c03970
ACS Catal. 2021, 11, 13496−13509

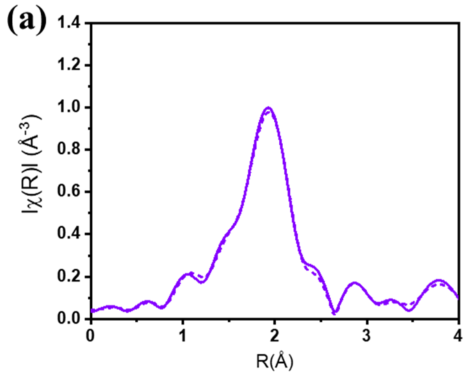

Figure 5. The k^2-weighted magnitudes of the FT of EXAFS spectra for (a) reduced (purple solid line) and oxidized (purple dashed line) Pt-P-20 and (b) reduced (blue solid line) and oxidized (blue dashed line) Pt-P-50.

is also confirmed by the DRIFT spectra of CO. Pt NPs readily absorb CO; while there are no DRIFT spectral peaks of PtP_2 exposed to CO (Figure S6). The lack of reactivity with RT air and the inability to absorb CO suggest that the chemical reactivity of PtP_2 is very different from that of Pt NPs.

Figure 6 shows the XANES spectra of the Pt−P samples together with Pt NPs. The XANES spectra of Pt/SiO_2 (black line) show that the shape, white line intensity, and edge energy are similar to those of the Pt foil, as shown in Figure S7. The edge energy was determined from the inflection of the leading edge of the XANES spectrum for all samples and is given in Table 1. For all Pt−P catalysts, the edge shifted to higher energies, and there is an increase in the intensity of the white line, that is, the first peak beyond the edge. The white line intensity is associated with ionization of the 2p electron to the unfilled Pt 5d orbitals, and an increased intensity is consistent with fewer electrons in 5d orbitals, that is, a higher oxidation state. As the amount of P in the catalysts increased, both the edge energy and the white line intensity increased slightly (Table 1). The maximum XANES edge energy shift of 1.5 eV and the maximum white line intensity were observed for the Pt-P-50 catalyst (PtP_2 NPs). Because Pt-P-20 and Pt-P-10 have core−shell structures, that is, contain both metallic Pt and PtP_2, the edge energies were slightly lower than that of Pt-P-50.

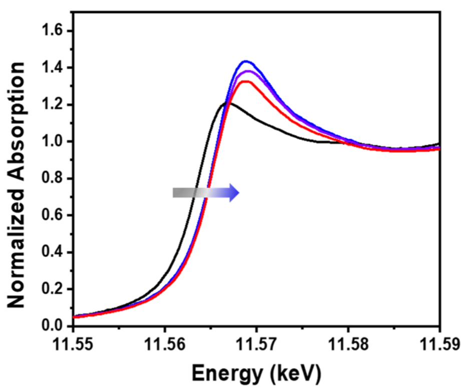

Figure 6. Normalized XANES spectra at the Pt L_3 edge of Pt/SiO_2 (black line), Pt-P-10 (red line), Pt-P-20 (purple line), and Pt-P-50 (blue line).

The XANES linear combination fitting for Pt-P-20 and Pt-P-10 was done to estimate the compositions of Pt and PtP_2 as shown in Figure S8 and Table S1. The Pt/SiO_2 and Pt-P-50 were used as the reference standards for the XANES fits. The fraction of metallic Pt is estimated to be 25 and 15% for Pt-P-10 and Pt-P-20, respectively.

One can estimate the volume of the Pt core from the fraction of Pt atoms by XANES, as well as the TEM size and size of the Pt unit cell. The Pt unit cell size is 0.392 nm, which gives a cell volume of 0.06 nm^3. The number of atoms in a NP of different sizes can be estimated by $4/3\pi R^3$. NPs of 1, 1.5, 2, and 2.5 nm have about 9, 29, 70, and 136 atoms, respectively. For NPs with about 20% of metallic atoms at the core, this would be about 27 atoms, or about 1.5 nm size. Thus, the shell is about 0.5 nm giving 2.5 nm PtP_2 on the Pt core. These estimates suggest a surface PtP_2 of about 2−3 atomic layers in the core−shell catalysts.

3.3. Chemical State of Pt in PtP_2 NPs. In situ XPS was employed to determine the oxidation state of Pt in the Pt−P catalysts, Figure 7. The Pt 4f region consists of two components, which correspond to two spin−orbital splitting peaks of Pt $4f_{7/2}$ (at lower binding energy) and Pt $4f_{5/2}$ (at higher binding energy). As a reference, Pt/SiO_2 exhibits a Pt $4f_{7/2}$ peak at 71.8 eV, which is assigned to metallic Pt. This value is higher than the binding energy of the Pt bulk metal of 71.0 eV, due to the decreased extra-atomic relaxation of small metal particles.[58] For Pt-P-50, the Pt $4f_{7/2}$ binding energy is 73.0 eV, 1.2 eV higher than that of Pt NPs, which can be

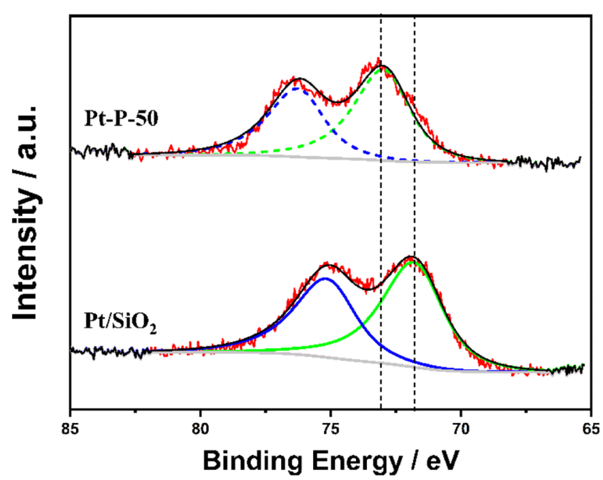

Figure 7. Pt 4f XPS spectra of catalysts after reduction at 550 °C with H_2. Raw data (red solid line), fitting curve (black solid line), Pt^0 state: Pt $4f_{7/2}$ (green solid line) and Pt^0 $4f_{5/2}$ (blue solid line), Pt^{2+} state: Pt $4f_{7/2}$ (green dashed line), and Pt $4f_{5/2}$ (blue dashed line).

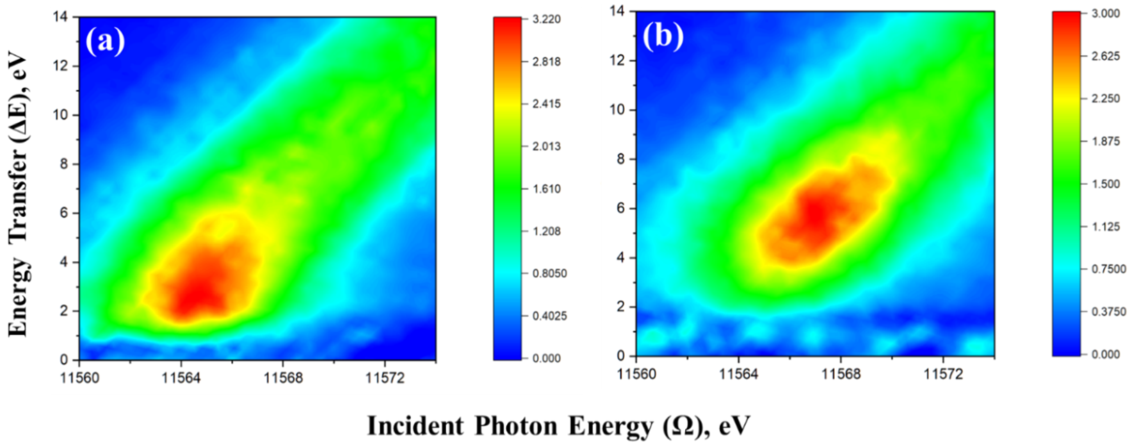

Figure 8. L_3 RIXS planes of (a) Pt/SiO_2 and (b) PtP_2/SiO_2.

attributed to Pt^{2+} in the NPs consistent with the shift to higher energy in the XANES spectra. In addition, the binding energy of the P 2p peak is 135.3 eV (Figure S9), indicating that the majority of P, which is present in large excess of that required to form PtP_2, are present as P^{5+}, likely P_2O_5.[59]

3.4. Determination of the Energy of the (Filled) Pt 5d Valence Orbitals. The XANES and XPS results suggest that the energy of the Pt 5d valence orbitals is significantly different from that of metallic Pt NPs. For example, the formation of PtP_2 increases the unfilled 5d orbital energies suggested by the L_{III} edge XANES. The increase in the 4f XPS binding energies also suggests a change in the energy of the Pt 5d valence orbitals. Both techniques, however, are indirect measurements of the energy of the filled 5d orbitals, which are primarily responsible for catalytic performance.[60] To directly quantify the effect of P on the energy of the filled valence states in PtP_2, in situ RIXS measurements were conducted on Pt/SiO_2 and PtP_2/SiO_2 (Pt-P-50), that is, where every Pt atom has the same structure. The energy difference between the unfilled and filled Pt 5d states was determined by the measurements of the L_3 absorption edge and $L\beta_5$ emission lines. Figure 8 shows the experimentally measured RIXS spectra for Pt/SiO_2 and PtP_2/SiO_2 as 2-D contour plot maps, where the energy transfer (ΔE), or the difference in average energy of the filled and unfilled 5d orbitals, is a function of the incident photon energy (Ω). The location of maximum intensity can be used to determine the difference between the average energies of the filled and unfilled 5d orbitals. The maximum intensity of Pt catalysts occurs at Ω = 11 564.4 eV with ΔE of 2.7 eV in accordance with literature.[61] Upon forming PtP_2, the maximum RIXS intensity shifts to a higher Ω of 11 567.0 eV and higher energy transfer, ca. $\Delta E \sim 5.7$, 3.0 eV larger than that in Pt NPs. Because the energy of unfilled valence states in PtP_2 was 1.5 eV higher than that in the monometallic Pt, determined by XANES in Figure 6, the energy of filled 5d valence orbitals in PtP_2 was 1.5 eV lower than that in Pt NPs. The schematics of the energy level diagram for Pt 5d valence bands in Pt/SiO_2 and PtP_2/SiO_2 are shown in Figure 9.

3.5. Catalytic Properties: Propane Dehydrogenation and Propylene Hydrogenation. The catalytic performance of PtP_2 and Pt NPs catalysts was determined for propylene hydrogenation and propane dehydrogenation. Because PtP_2 did not adsorb CO at RT as confirmed by CO-IR (Figure S6), it was not possible to determine the fraction of surface Pt using standard chemisorption methods. However, the average

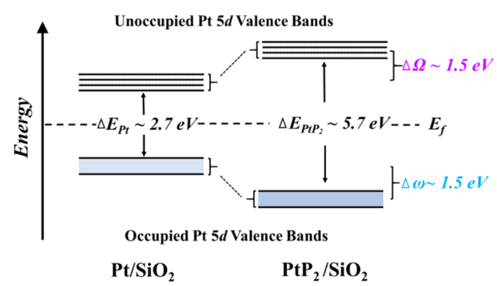

Figure 9. Schematics of the energy level diagram for Pt 5d valence bands in Pt/SiO_2 and PtP_2/SiO_2.

particle size and size distributions of Pt NPs and PtP_2 NPs (Pt-P-50) are similar, and these two catalysts have uniform compositions. Thus, the number of surface Pt sites in Pt and Pt-P-50 per gram catalyst should be very similar, and the rate per mol Pt can be used to evaluate the relative rates of Pt in these catalysts.

The rates per g of Pt for the Pt−P catalysts for propylene hydrogenation and propane dehydrogenation are given in Table 2. There was no propylene conversion with Pt-P-50 until the temperature was higher than about 150 °C, which is consistent with other single-site catalysts, for example, Co(II),[62] Zn(II),[63] and Ga(III);[64] while Pt/SiO_2 is highly active at RT consistent with metallic Pt.[65,66] The rates of Pt NPs and Pt-P-50 for hydrogenation were calculated at a conversion of ∼10% at 150 °C. The rate of Pt NPs is about 900 times higher than that of PtP_2 (Pt-P-50). The much lower rate of PtP_2 than metallic NPs for hydrogenation is also consistent with the rates of other single-site catalysts, for example, single-site Zn(II)/SiO_2 (Table 2).

Because alkane dehydrogenation is the reverse reaction of olefin hydrogenation, PtP_2 catalysts were evaluated for the former reaction. The conversion and selectivity on P/SiO_2 and SiO_2 are also shown in Figure S10. The performance of P/SiO_2 was almost the same as that of SiO_2, which had little contribution to the catalytic performances. Figure 10 shows the initial selectivity versus conversion of these supported Pt catalysts for PDH reactions at 550 °C. The addition of H_2 to the reaction gases is a more severe test of the catalyst performance because H_2 promotes the hydrogenolysis reaction. The selectivity of the reference Pt/SiO_2 catalyst decreased rapidly from 82 to 63% as the conversion increased from 8 to 27%, which is consistent with the literature.[4,6] By

https://doi.org/10.1021/acscatal.1c03970
ACS Catal. 2021, 11, 13496−13509

Table 2. Catalytic Performance in Propylene Hydrogenation at 150 °C in 3% C_3H_6, 5% H_2 Balance with N_2 and Propane Dehydrogenation at 550 °C in 5% C_3H_8, and 5% H_2 Balance with N_2

catalyst	rate of hydrogenation ($mol_{C_3H_6}$/mol M s^{-1})	rate of dehydrogenation ($mol_{C_3H_8}$/mol M·s^{-1})	selectivity (%)[a]	k_d (h^{-1})
Pt/SiO_2	2.7	8.8×10^{-2}	64	0.182
Pt-P-10	5.3×10^{-3}	1.9×10^{-2}	97	
Pt-P-20	3.4×10^{-3}		96	
Pt-P-50	3.2×10^{-3}	1.2×10^{-2}	97	0.147
Zn(II)/SiO_2[63]	8.4×10^{-5}	2.1×10^{-4}	>95	
Co(II)/SiO_2[62]		1.8×10^{-4}	>95	
Ga(III)//SiO_2[64]		5.4×10^{-4}	>98	

[a]Selectivity: propylene selectivity at 25% conversion of propane for Pt−P catalysts.

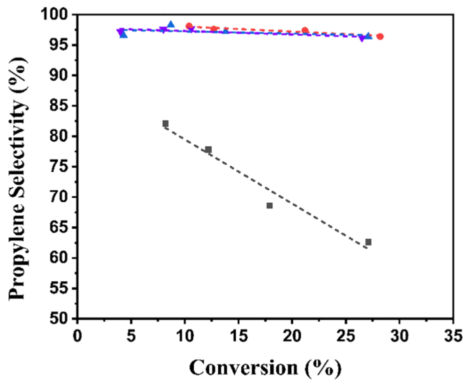

Figure 10. Initial selectivity vs conversion in PDH after reduction at 550 °C in 5% C_3H_8, 5% H_2 balance with N_2 for Pt/SiO_2 (black), Pt-P-10 (red), Pt-P-20 (purple), and Pt-P-50 (blue).

contrast, all the Pt−P catalysts show significantly improved olefin selectivity, generally above 95%, up to ∼30% conversion, as shown in Figure 10. The selectivity of these Pt catalysts at 25% conversion is listed in Table 2 for comparison. For the Pt-P-50 catalyst, the propylene selectivity remains about 97% at 25% propane conversion. Pt-P-10 and Pt-P-20 show a similar performance to Pt-P-50, where the selectivity remains above 96% at 25% conversion, which suggests that the surfaces of Pt-P-10 and Pt-P-20 are likely similar to that of Pt-P-50.

The rates per mole Pt (based on 2 wt % Pt) for PDH were calculated at 550 °C at around 10% conversion, as shown in Table 2. The propane conversion rate of Pt/SiO_2 is 0.088 mol C_3H_8/mol Pt s^{-1}, is about seven times higher than 0.012 mol C_3H_8/mol Pt s^{-1} of the PtP_2 (Pt-P-50) catalyst. The lower rates and high selectivity of Pt−P catalysts are again consistent with those of the reported transition metal[62,64,67] and main group[62,64,67] single site-catalysts, as shown in Table 2.

The stability of Pt and PtP_2 (Pt-P-50) was also evaluated assuming a first-order deactivation mechanism, and the deactivation rate constants (k_d) are listed in Table 2. Figure S11 shows the propane conversion versus time-on-stream over Pt NPs and Pt-P-50 catalysts, where the initial conversion of both catalysts was ∼28%. For both Pt NPs and Pt-P-50, the conversion declined rapidly over the first 30 min and stabilized after 5 h. The k_d of Pt-P-20 is 0.147 h^{-1}, which is slightly lower than 0.182 h^{-1} of Pt NPs. The synthesis conditions of PtP_2 have not been optimized for deactivation, and alkali addition to other metal phosphides has been shown to reduce acid sites from excess phosphate and improve conversion stability.[46,68]

3.6. Selective Acetylene Hydrogenation. Hydrogenation of acetylene yields ethylene, which can be further hydrogenated to ethane. A selective catalyst will be able to provide high concentrations of ethylene. The selectivity defined in eq 6 of the experimental section indicates the ability of the catalyst to suppress the overhydrogenation to form ethane. 1 wt % Pd/alumina was used as a reference catalyst because Pd is known to be effective for selective

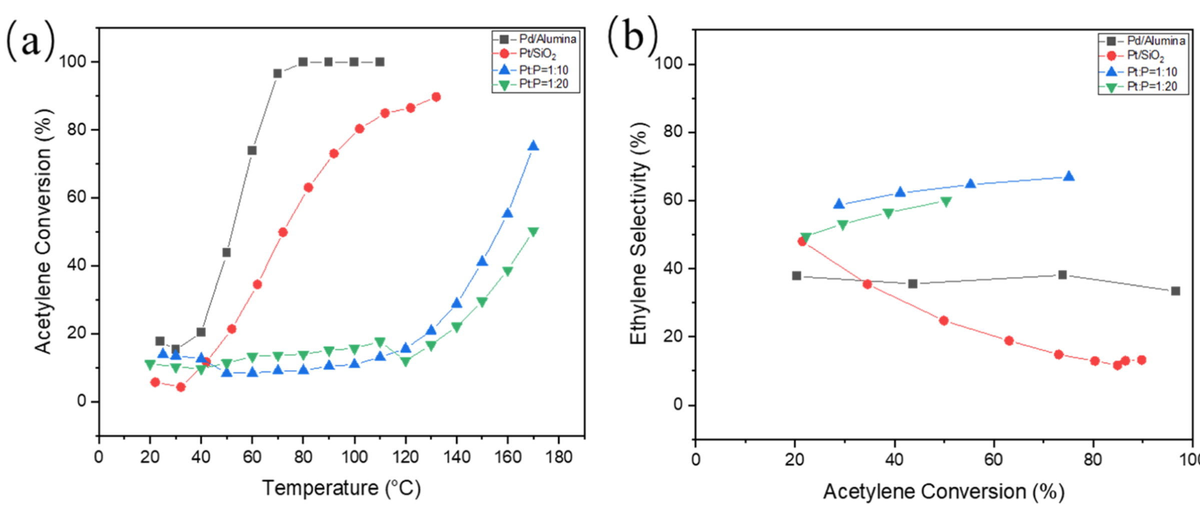

Figure 11. Catalysts Pd/Al_2O_3 (grey), Pt/SiO_2 (red), Pt-P-10 (blue), and Pt-P-20 (green) were reduced in 4% H_2 balance with N_2 at 350 °C for 60 min and then a feed stream of 1% C_2H_2, 4% H_2, and the rest balanced with N_2 for selective acetylene hydrogenation. (a) Acetylene conversion as a function of temperature and (b) ethylene selectivity as a function of acetylene conversion.

https://doi.org/10.1021/acscatal.1c03970
ACS Catal. 2021, 11, 13496−13509

hydrogenation of acetylene to ethylene for the production of polymer grade ethylene[69]. On the other hand, metallic Pt is not known to be highly selective for acetylene hydrogenation. Figure 11a shows the conversion of acetylene as a function of temperature and increasing conversion. Figure S12 shows the concentrations of acetylene, ethylene, and ethane for each catalyst, and the ethylene selectivity as a function of acetylene conversion is shown in Figure 11b. Metallic Pt is active at temperatures from 40 to 140 °C, but the selectivity to ethylene is low and shows a monotonic decrease with increasing conversion. For the PtP_2 catalysts, hydrogenation occurs at higher temperatures due to their lower intrinsic activity, but ethylene selectivity is significantly higher than that of Pt and even Pd NPs. In addition, the selectivity remains high at higher conversions. Table 3 shows the selectivity of these catalysts at

Table 3. Catalytic Results of Selective Acetylene Hydrogenation

catalyst	T_{50} (°C)[a]	ethylene selectivity (%)[b]
Pd/Al_2O_3	52	36
Pt/SiO_2	72	25
Pt-P-10	155	63
Pt-P-20	170	60

[a]Catalyst bed outlet temperature for 50% acetylene conversion. [b]Ethylene selectivity at 50% acetylene conversion.

50% conversion of acetylene, showing the improvement attained with the PtP_2 catalysts. The loss in selectivity for Pt NPs can be attributed to the strong binding of ethylene on metallic Pt with facile hydrogenation to form ethane. While in the case of PtP_2, where Pt is present in the +2 oxidation state, weaker binding of ethylene allows it to desorb, leading to improved overall selectivity. Figure 11b clearly shows that the PtP_2 catalysts retain their selectivity toward ethylene at high conversions of acetylene, which is required because acetylene is a poison for the downstream polymerization catalysts.[70]

4. DISCUSSION

4.1. Synthesis and Formation of PtP_2. PtP_2 was previously prepared by dissociating an organometallic precursor at 1000−1100 °C, resulting in large particles of ∼50 nm.[71] In our study, supported PtP_2 NPs with a particle size of 2−3 nm were prepared with different amounts of H_3PO_4 by IWI following a reduction at 550 °C, which is similar to industrial synthesis methods. The cheap, safe, and readily available phosphorus source and the relatively low reduction temperature are suitable for largescale preparations. After calcination, the oxidized Pt NPs were formed. The EXAFS spectrum of unreduced Pt-P-50 was well fitted with Pt−O scattering (Figure S13). After H_2 reduction at 550 °C, the PtP_2 ordered structure was formed confirmed by EXAFS and STEM. Here, the Pt^{2+} ions in PtP_2 are formed in a high-temperature reducing environment in agreement with the reported synthesis conditions for other phosphorus-rich transition-metal phosphides (MP_2/MP_3).[71−73] During the reduction, it is likely that Pt ions dissociate H_2, which facilitates the reduction of phosphate through hydrogen spillover.[74]

In addition to full PtP_2, Pt-P-10 and Pt-P-20 display a core−shell structure (Pt@PtP_2) confirmed by EXAFS, sXRD, surface XAS, and catalytic performance. As the P/Pt molar ratio increases from 10 to 20, the CN_{Pt-Pt} decreases from 2.4 to 1.8 and the CN_{Pt-P} increases from 3.5 to 3.7. We hypothesize that in a reducing environment, Pt NPs were initially formed, and then the phosphorus diffuses from the surface to the center of the particle to form PtP_2 with Pt atoms. The more the amount of phosphorus, the more the surface PtP_2 formation was until the NP consists of pure PtP_2, as shown in Figure 12. For all

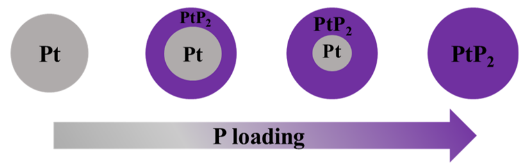

Figure 12. Schematics of the evolution of the NP structure with the increase of P loading.

catalysts, there is a large excess of P than is required for the formation of PtP_2. The excess P is present at P^{5+} as determined by XPS. This also suggests phosphate ions, which are not near the initially formed Pt NPs, cannot be reduced under these conditions. The same surface of Pt@PtP_2 and pure PtP_2 NPs leads to a similar catalytic performance, for example, a low rate per mole Pt (compared to Pt NPs), high olefin selectivity, no CO chemisorption capacity, etc.

4.2. Nature of Surface Pt^{2+} Ions in PtP_2 NPs. Pt-P-50 has a fully formed PtP_2 crystalline structure with Pt−P bonds at 2.36 Å, as confirmed by EXAFS (Figure 1) and STEM (Figure 4). As shown in Figure 13, in the PtP_2 structure, Pt still

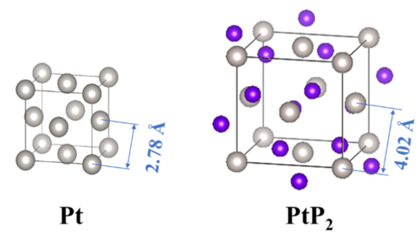

Figure 13. Unit cell of Pt fcc and PtP_2 crystalline structure (Pt atoms are represented in gray and P atoms in purple).

adopts a fcc unit cell, albeit with a much larger size than Pt NPs, with P_2^{2-} ions midway between the Pt^{2+} ions. The Pt−Pt distance is 4.02 Å, significantly longer than that in Pt NPs (2.78 Å). In PtP_2, the distance between adjacent Pt is too long for Pt−Pt bond formation.

The increase of white line intensity and edge energy of XANES is consistent with Pt^{2+} in PtP_2, which agrees with Pt^{2+} binding energies determined by XPS. The energy of Pt valence orbitals, which form bonds with reactants and products, determines the catalytic properties. To directly quantify and compare the energy of the filled 5d valence orbitals, RIXS was conducted on Pt NPs and the full-phase PtP_2. RIXS is a bulk technique and measures every atom in the sample. Thus, it is essential that each Pt has an identical structure. As shown in the XANES spectrum, Figure 6, the formation of PtP_2 significantly increases the energy of unfilled Pt 5d orbitals by 1.5 eV. The RIXS spectrum is the difference in energy of the empty and filled Pt 5d states. Thus, there is a decrease in the energy of filled Pt 5d orbitals by 1.5 eV, Figures 8 and 9, compared to Pt NPs. The increase in the energy of unfilled orbitals is nearly the same as the decrease in the energy of the filled orbitals, which is similar to previously studied bimetallic

https://doi.org/10.1021/acscatal.1c03970
ACS Catal. 2021, 11, 13496−13509

Pt catalysts.[5,6] For comparison, the decrease in energy of the filled 5d orbitals in PtP_2 NPs is larger than those observed for many bimetallic Pt catalysts, for example, a 1.1 eV shift for Pt_1Zn_1[5] and a 0.4 eV shift for Pt_3V[61] catalysts. This decrease in the energy of the filled 5d orbitals in PtP_2 would be expected to lead to significantly weaker Pt-adsorbate and reaction intermediate bond energies compared to metallic Pt.

4.3. Structure−Property Relationship and Implications for Catalysis. Pt is one of the most versatile catalytic elements with applications to both oxidation and reduction reactions, for example, hydrocarbon and CO oxidation, olefin hydrogenation, naphtha reforming, fuel cells, electrocatalysis, etc.[1,75] In each of these, metallic Pt is the active phase. Although phosphorous-rich metal phosphides are known, currently all catalytically active transition-metal phosphides are metal-rich and possess metallic properties.[35,38] Metal-rich transition-metal phosphides have MP and M_2P structures. For example, Oyama[40] has compared the hydrodesulfurization, hydrodenitrogenation, and hydrodeoxygenation activity for a series of metal phosphide catalysts, and the activity increased in the order, Fe_2P < CoP < MoP < WP < Ni_2P. By comparison, PtP_2 was much less active than other metal phosphide catalysts, although the reason for the very low activity was not known.[39] As shown above, PtP_2 is not metallic and does not show catalytic or chemisorption properties typical of Pt NPs. For example, PtP_2 does not hydrogenate olefins at low temperature, chemisorb CO, and is not oxidized by air at low temperature. The Pt^{2+} surface ions, however, catalyze olefin hydrogenation but at much higher temperature than Pt NPs, and will affect alkane dehydrogenation, albeit at a lower turnover rate than metallic Pt. While PtP_2 has a lower rate than Pt NPs, it does have significantly improved selectivity. For propane dehydrogenation, Pt is poorly selective, ca. 65% at 20% conversion, while the olefin selectivity of PtP_2 is greater than 95% at the same conversion. Similarly, the selectivity for acetylene hydrogenation to ethylene is much higher for PtP_2 than Pt NPs. The catalytic properties of PtP_2 are less like those of Pt NPs and more similar to those of single-site, ionic catalysts, for example, single-site Co(II),[62] Zn(II),[63] and Ga(III)[64] ions on silica and Ga[26,76] and Cr[77] on alumina. For the latter, however, the structures and composition of the catalytic sites are significantly different from that in PtP_2. In the transition and main group catalysts, the active site is a low coordinate, isolated ion bonded to and stabilized by the support, that is, a metal ion is bonded through support O ions. For all the non-metallic dehydrogenation catalysts, the oxides are not reduced to metallic NPs at the high reaction temperatures. In PtP_2, while the Pt^{2+} ions are isolated from other Pt ions, that is, no Pt−Pt bonds, they are not bonded to the support but are present in a nanoparticle. Thus, for the maximum rate, it is necessary to synthesize small NPs. Similar to the active sites in Zn(II),[63,78] Co(II),[62] Ga(III),[64] and Fe(II)[79] single-site catalysts, PtP_2 does not reduce to metallic NPs due to stabilization of the Pt^{2+} ions by the P_2^{2-} ions. Thus, PtP_2 can be used for high-temperature hydrogenation reactions.

Single-site Zn(II),[63,78] Co(II),[62] Ga(III),[64] and Fe(II)[79] supported on silica catalysts also show olefin selectivities above about 95% and often with little coke formation or lower deactivation rates than bimetallic alloy NPs.[63,79] Although non-metallic dehydrogenation catalysts have high olefin selectivity and, generally, suppressed coke formation, a limitation of these catalysts is their lower rate compared to metallic catalysts. The olefin hydrogenation and alkane dehydrogenation rates of Pt^{2+} in PtP_2 are about 40 and 90 times higher, respectively, than those for Zn(II)/SiO_2 single-site catalysts, Table 2. For the latter, all sites are active; while in PtP_2 about 40% of the Pt would be at the surface of the 2.5 nm particles. Thus, the turnover rate (TOR) of Pt^{2+} is approximately 100 times higher for olefin hydrogenation and over 200 times higher for propane dehydrogenation than those of Zn(II)/SiO_2.

The difference in adsorption energies, reaction rates, and selectivity compared to metallic Pt NPs also suggests that PtP_2 catalysts may find different catalytic applications than the former. The results for selective hydrogenation of acetylene over ethylene are consistent with this suggestion. Although Pt NPs are highly active for acetylene and ethylene hydrogenation, the poor selectivity is likely due to strong bonding of the product ethylene to metallic Pt, and high surface coverage of activated hydrogen leads to the overhydrogenation of the ethylene (to ethane) resulting in poor selectivity. For PtP_2, the isolated Pt^{2+} leads to weak bonding of the ethylene and also low hydrogen coverage of the NP resulting in improved selectivity.

The development of new, single-site, ionic catalytic materials for a variety of catalytic applications in electrocatalysis, photocatalysis, thermal catalysis, is an active area of research.[80,81] These often display catalytic properties, which are distinct from those of metal NPs. For these catalysts, the ions are generally stabilized by the oxide, carbon or carbon−nitrogen support.[82−84] Here, we show that active single-site ions present in nanoparticles with chemically stable molecular structures can also be considered possible new materials for these and other reactions. While further improvements in rate, selectivity, and stability may be required for technological applications of PtP_2, the results do demonstrate the opportunity for its better performance for some reactions compared to metallic Pt NPs. The chemistry of PtP_2 and similar nanoparticle single-site, ionic catalysts remains to be explored, but it is anticipated that the preferred reactions will be different from those of metallic NPs.

5. CONCLUSIONS

Silica-supported 2−3 nm PtP_2 NPs were successfully synthesized using a simple and scalable IWI method. In the PtP_2 NPs, the Pt^{2+} ions are separated by P_2^{2-} ions, that is, no Pt−Pt bonds, unlike other Group 8 catalytic metal phosphide catalysts, for example, Ni, Fe, Ru, and Rh. In PtP_2, the energy of the filled Pt 5d valence orbitals is about 1.5 eV lower than that in metallic Pt NPs. These electronic effects lead to a decrease in bond strength of adsorbates, for example, CO and reaction intermediates, lowering the rates but also improving the selectivity. The PtP_2 catalytic surface exhibits very low hydrogenation rates nearly 1000 times lower than that of metallic Pt requiring higher reaction temperatures. At higher temperatures, the propane dehydrogenation rate per Pt in PtP_2 is about 7 times lower than that in Pt NPs; however, the former has excellent olefin selectivity compared to the latter. The difference in rates and selectivity suggests that PtP_2 will find different applications to those of Pt NPs as demonstrated by the selective hydrogenation of acetylene. The isolated Pt^{2+} ions have a significantly higher turnover rate than other ionic and alloy single-site catalysts and thus may have potential for similar applications of the latter.

https://doi.org/10.1021/acscatal.1c03970
ACS Catal. 2021, 11, 13496−13509

ASSOCIATED CONTENT

Supporting Information

The Supporting Information is available free of charge at https://pubs.acs.org/doi/10.1021/acscatal.1c03970.

Quality of EXAFS fits; k^3-weighting magnitudes of the FT of the EXAFS spectra for Pt and Pt−P NPs; XRD patterns and P XPS of Pt-P-50; EXAFS spectra of the reduced and unreduced Pt-P-50; normalized XANES spectra of reduced and oxidized Pt−P catalysts; normalized XANES spectra and linear combination fitting results of Pt-P-10 and Pt-P-20; catalytic performance of PDH for Pt/SiO_2 and P/SiO_2; propane conversion versus time for Pt/SiO_2 and Pt-P-50; and GC results for selective acetylene hydrogenation (PDF)

AUTHOR INFORMATION

Corresponding Authors

Guanghui Zhang − *State Key Laboratory of Fine Chemicals, PSU-DUT Joint Center for Energy Research, School of Chemical Engineering, Dalian University of Technology, Dalian 116024, China;* orcid.org/0000-0002-5854-6909; Email: gzhang@dlut.edu.cn

Liejin Guo − *State Key Laboratory of Multiphase Flow in Power Engineering, Xi'an Jiaotong University, Xi'an 710049, China;* orcid.org/0000-0001-9412-3260; Email: lj-guo@mail.xjtu.edu.cn

Jeffrey T. Miller − *Davidson School of Chemical Engineering, Purdue University, West Lafayette, Indiana 47907, United States;* orcid.org/0000-0002-6269-0620; Email: mill1194@purdue.edu

Authors

Jiajing Kou − *State Key Laboratory of Multiphase Flow in Power Engineering, Xi'an Jiaotong University, Xi'an 710049, China; Davidson School of Chemical Engineering, Purdue University, West Lafayette, Indiana 47907, United States*

Johnny Zhu Chen − *Davidson School of Chemical Engineering, Purdue University, West Lafayette, Indiana 47907, United States;* orcid.org/0000-0003-0697-4351

Junxian Gao − *Davidson School of Chemical Engineering, Purdue University, West Lafayette, Indiana 47907, United States;* orcid.org/0000-0002-1015-7103

Xiaoben Zhang − *Dalian National Laboratory for Clean Energy, Dalian Institute of Chemical Physics, Chinese Academy of Sciences, Dalian 116023, China*

Jie Zhu − *State Key Laboratory of Fine Chemicals, PSU-DUT Joint Center for Energy Research, School of Chemical Engineering, Dalian University of Technology, Dalian 116024, China;* orcid.org/0000-0003-0651-8022

Arnab Ghosh − *Department of Chemical and Biological Engineering, University of New Mexico, Albuquerque, New Mexico 87131, United States*

Wei Liu − *Dalian National Laboratory for Clean Energy, Dalian Institute of Chemical Physics, Chinese Academy of Sciences, Dalian 116023, China;* orcid.org/0000-0002-4403-737X

A. Jeremy Kropf − *Chemical Science and Engineering Division, Argonne National Laboratory, Lemont, Illinois 60439, United States*

Dmitry Zemlyanov − *Birck Nanotechnology Center, Purdue University, West Lafayette, Indiana 47907, United States;* orcid.org/0000-0002-1221-9195

Rui Ma − *Chemistry and Chemical Engineering Guangdong Laboratory, Shantou 515031, China*

Xinwen Guo − *State Key Laboratory of Fine Chemicals, PSU-DUT Joint Center for Energy Research, School of Chemical Engineering, Dalian University of Technology, Dalian 116024, China*

Abhaya K. Datye − *Department of Chemical and Biological Engineering, University of New Mexico, Albuquerque, New Mexico 87131, United States;* orcid.org/0000-0002-7126-8659

Complete contact information is available at: https://pubs.acs.org/10.1021/acscatal.1c03970

Notes

The authors declare no competing financial interest.

ACKNOWLEDGMENTS

J.K. and L.G. were supported by the Basic Science Center Program for Ordered Energy Conversion of the National Natural Science Foundation of China (no. 51888103). J.K. also wishes to thank the China Scholarship Council (201806280119). J.Z.C., G.Z., A.G., A.K.D., and J.T.M. were supported in part by the National Science Foundation under Cooperative Agreement no. EEC-1647722. J.G., D.Z., and J.T.M. were supported by the National Science Foundation under award CBET-1804712. A.G. and A.K.D. were supported by the NSF GOALI grant CBET 1707127. G.Z. would like to acknowledge the National Natural Science Foundation of China (21902019) and Fundamental Research Funds for the Central Universities (DUT20RC(5)002). W.L. acknowledges the CAS Youth Innovation Promotion Association (2019190). R.M. would like to thank Chemistry and Chemical Engineering Guangdong Laboratory for a startup funding support (2111001). A.J.K. was supported by the U.S. Department of Energy (DOE), Office of Basic Energy Sciences, Division of Chemical Sciences, Geosciences, and Biosciences, Catalysis Science Program under Contract DE-AC02-06CH11357 (Argonne National Laboratory). Use of the Advanced Photon Source was supported by the U.S. Department of Energy Office of Basic Energy Sciences under contract no. DE-AC02-06CH11357. MRCAT operations, beamlines 10-BM and 10-ID, were supported by the Department of Energy and the MRCAT member institutions. The authors also acknowledge the use of beamline 11-ID-C.

REFERENCES

(1) Yu, W.; Porosoff, M. D.; Chen, J. G. Review of Pt-Based Bimetallic Catalysis: From Model Surfaces to Supported Catalysts. *Chem. Rev.* **2012**, *112*, 5780−5817.

(2) Cortright, R. D.; Dumesic, J. A. Effects of potassium on silica-supported Pt and Pt/Sn catalysts for isobutane dehydrogenation. *J. Catal.* **1995**, *157*, 576−583.

(3) Sattler, J. J. H. B.; Ruiz-Martinez, J.; Santillan-Jimenez, E.; Weckhuysen, B. M. Catalytic dehydrogenation of light alkanes on metals and metal oxides. *Chem. Rev.* **2014**, *114*, 10613−10653.

(4) LiBretto, N. J.; Yang, C.; Ren, Y.; Zhang, G.; Miller, J. T. Identification of Surface Structures in Pt_3Cr Intermetallic Nanocatalysts. *Chem. Mater.* **2019**, *31*, 1597−1609.

(5) Cybulskis, V. J.; Bukowski, B. C.; Tseng, H.-T.; Gallagher, J. R.; Wu, Z.; Wegener, E.; Kropf, A. J.; Ravel, B.; Ribeiro, F. H.; Greeley, J.; Miller, J. T. Zinc Promotion of Platinum for Catalytic Light Alkane Dehydrogenation: Insights into Geometric and Electronic Effects. *ACS Catal.* **2017**, *7*, 4173−4181.

(6) Cesar, L. G.; Yang, C.; Lu, Z.; Ren, Y.; Zhang, G.; Miller, J. T. Identification of a Pt_3Co Surface Intermetallic Alloy in Pt-Co Propane Dehydrogenation Catalysts. *ACS Catal.* **2019**, *9*, 5231−5244.
(7) Zhu Chen, J.; Wu, Z.; Zhang, X.; Choi, S.; Xiao, Y.; Varma, A.; Liu, W.; Zhang, G.; Miller, J. T. Identification of the Structure of the Bi Promoted Pt Non-oxidative Coupling of Methane Catalyst: A Nanoscale Pt_3Bi Intermetallic Alloy. *Catal. Sci. Technol.* **2019**, *9*, 1349−1356.
(8) Ye, C.; Wu, Z.; Liu, W.; Ren, Y.; Zhang, G.; Miller, J. T. Structure Determination of a Surface Tetragonal Pt_1Sb_1 Phase on Pt Nanoparticles. *Chem. Mater.* **2018**, *30*, 4503−4507.
(9) Wegener, E. C.; Wu, Z.; Tseng, H.-T.; Gallagher, J. R.; Ren, Y.; Diaz, R. E.; Ribeiro, F. H.; Miller, J. T. Structure and reactivity of Pt−In intermetallic alloy nanoparticles: Highly selective catalysts for ethane dehydrogenation. *Catal. Today* **2018**, *299*, 146−153.
(10) Zhu, H.; Anjum, D. H.; Wang, Q.; Abou-Hamad, E.; Emsley, L.; Dong, H.; Laveille, P.; Li, L.; Samal, A. K.; Basset, J.-M. Sn surface-enriched Pt−Sn bimetallic nanoparticles as a selective and stable catalyst for propane dehydrogenation. *J. Catal.* **2014**, *320*, 52−62.
(11) Chen, S.; Chang, X.; Sun, G.; Zhang, T.; Xu, Y.; Wang, Y.; Pei, C.; Gong, J. Propane dehydrogenation: catalyst development, new chemistry, and emerging technologies. *Chem. Soc. Rev.* **2021**, *50*, 3315−3354.
(12) Rahimpour, M. R.; Jafari, M.; Iranshahi, D. Progress in catalytic naphtha reforming process: A review. *Appl. Energy* **2013**, *109*, 79−93.
(13) Ciapetta, F. G.; Wallace, D. N. Catalytic naphtha reforming. *Catal. Rev. Sci. Eng.* **1972**, *5*, 67−158.
(14) Schweitzer, N. M.; Schaidle, J. A.; Ezekoye, O. K.; Pan, X.; Linic, S.; Thompson, L. T. High activity carbide supported catalysts for water gas shift. *J. Am. Chem. Soc.* **2011**, *133*, 2378.
(15) Li, Y.; Kottwitz, M.; Vincent, J. L.; Enright, M. J.; Liu, Z.; Zhang, L.; Huang, J.; Senanayake, S. D.; Yang, W.-C. D.; Crozier, P. A.; Nuzzo, R. G.; Frenkel, A. I. Dynamic structure of active sites in ceria-supported Pt catalysts for the water gas shift reaction. *Nat. Commun.* **2021**, *12*, 914.
(16) Cortright, R. D.; Davda, R. R.; Dumesic, J. A. Hydrogen from catalytic reforming of biomass-derived hydrocarbons in liquid water. *Nature* **2002**, *418*, 964−967.
(17) Shelef, M.; Mccabe, R. W. Twenty-five years after introduction of automotive catalysts: what next? *Catal. Today* **2000**, *62*, 35−50.
(18) Farrauto, R. J.; Heck, R. M. Catalytic converters: state of the art and perspectives. *Catal. Today* **1999**, *51*, 351−360.
(19) Sui, S.; Wang, X.; Zhou, X.; Su, Y.; Riffat, S.; Liu, C. J. A comprehensive review of Pt electrocatalysts for the oxygen reduction reaction: Nanostructure, activity, mechanism and carbon support in PEM fuel cells. *J. Mater. Chem. A* **2017**, *5*, 1808−1825.
(20) Zhu, J.; Hu, L.; Zhao, P.; Lee, L. Y. S.; Wong, K.-Y. Recent Advances in Electrocatalytic Hydrogen Evolution Using Nanoparticles. *Chem. Rev.* **2019**, *120*, 851−918.
(21) Shrestha, S.; Liu, Y.; Mustain, W. E. Electrocatalytic Activity and Stability of Pt clusters on State-of-the-Art Supports: A Review. *Cat. Rev.—Sci. Eng.* **2011**, *53*, 256−336.
(22) Bariås, O. A.; Holmen, A.; Blekkan, E. A. Propane dehydrogenation over supported Pt and Pt−Sn catalysts: catalyst preparation, characterization, and activity measurements. *J. Catal.* **1996**, *158*, 1−12.
(23) Zhang, Y.; Zhou, Y.; Qiu, A.; Wang, Y.; Xu, Y.; Wu, P. Propane dehydrogenation on PtSn/ZSM-5 catalyst: Effect of tin as a promoter. *Catal. Commun.* **2006**, *7*, 860−866.
(24) Airaksinen, S. M. K.; Harlin, M. E.; Krause, A. O. I. Kinetic modeling of dehydrogenation of isobutane on chromia/alumina catalyst. *Ind. Eng. Chem. Res.* **2002**, *41*, 5619−5626.
(25) Puurunen, R.; Weckhuysen, B. M. Spectroscopic study on the irreversible deactivation of chromia/alumina dehydrogenation catalysts. *J. Catal.* **2002**, *210*, 418−430.
(26) Sattler, J. J. H. B.; Gonzalez-Jimenez, I. D.; Luo, L.; Stears, B. A.; Malek, A.; Barton, D. G.; Kilos, B. A.; Kaminsky, M. P.; Verhoeven, T. W. G. M.; Koers, E. J.; Baldus, M.; Weckhuysen, B. M. Platinum-Promoted Ga/Al2O3 as Highly Active, Selective, and Stable Catalyst for the Dehydrogenation of Propane. *Angew* **2014**, *53*, 9251−9256.
(27) Prins, R.; Bussell, M. E. Metal phosphides: preparation, characterization and catalytic reactivity. *Catal. Lett.* **2012**, *142*, 1413−1436.
(28) Yuan, C.-Z.; Hui, K. S.; Yin, H.; Zhu, S.; Zhang, J.; Wu, X.-L.; Hong, X.; Zhou, W.; Fan, X.; Bin, F.; Chen, F.; Hui, K. N. Regulating Intrinsic Electronic Structures of Transition-Metal-Based Catalysts and the Potential Applications for Electrocatalytic Water Splitting. *Acs Mater. Lett.* **2021**, *3*, 752−780.
(29) El-Refaei, S. M.; Russo, P. A.; Pinna, N. Recent Advances in Multimetal and Doped Transition-Metal Phosphides for the Hydrogen Evolution Reaction at Different pH values. *ACS Appl. Mater. Interfaces* **2021**, *13*, 22077−22097.
(30) Shi, Y.; Li, M.; Yu, Y.; Zhang, B. Recent advances in nanostructured transition metal phosphides: synthesis and energy-related applications. *Energy Environ. Sci.* **2020**, *13*, 4564−4582.
(31) Pu, Z.; Liu, T.; Amiinu, I. S.; Cheng, R.; Wang, P.; Zhang, C.; Ji, P.; Hu, W.; Liu, J.; Mu, S. Transition-metal phosphides: activity origin, energy-related electrocatalysis applications and synthetic strategies. *Adv. Funct. Mater.* **2020**, *30*, 2004009.
(32) Alvarado Rupflin, L.; Boscagli, C.; Schunk, S. Platinum group metal phosphides as efficient catalysts in hydroprocessing and syngas-related catalysis. *Catalysts* **2018**, *8*, 122.
(33) Feng, L.; Xue, H. Advances in Transition-Metal Phosphide Applications in Electrochemical Energy Storage and Catalysis. *Chemelectrochem* **2017**, *4*, 20−34.
(34) Liu, K.; Zhang, C.; Sun, Y.; Zhang, G.; Shen, X.; Zou, F.; Zhang, H.; Wu, Z.; Wegener, E. C.; Taubert, C. J.; Miller, J. T.; Peng, Z.; Zhu, Y. High-performance transition metal phosphide alloy catalyst for oxygen evolution reaction. *ACS Nano* **2018**, *12*, 158−167.
(35) Shi, Y.; Zhang, B. Recent advances in transition metal phosphide nanomaterials: synthesis and applications in hydrogen evolution reaction. *Chem. Soc. Rev.* **2016**, *45*, 1529−1541.
(36) Pei, Y.; Cheng, Y.; Chen, J.; Smith, W.; Dong, P.; Ajayan, P. M.; Ye, M.; Shen, J. Recent developments of transition metal phosphides as catalysts in the energy conversion field. *J. Mater. Chem. A* **2018**, *6*, 23220−23243.
(37) Zhao, H. Y.; Li, D.; Bui, P.; Oyama, S. T. Hydrodeoxygenation of guaiacol as model compound for pyrolysis oil on transition metal phosphide hydroprocessing catalysts. *Appl. Catal. A: Gen.* **2011**, *391*, 305−310.
(38) Oyama, S. T.; Gott, T.; Zhao, H.; Lee, Y.-K. Transition metal phosphide hydroprocessing catalysts: A review. *Catal. Today* **2009**, *143*, 94−107.
(39) Kanda, Y.; Temma, C.; Nakata, K.; Kobayashi, T.; Sugioka, M.; Uemichi, Y. Preparation and performance of noble metal phosphides supported on silica as new hydrodesulfurization catalysts. *Appl. Catal., A* **2010**, *386*, 171−178.
(40) Oyama, S. T. Novel catalysts for advanced hydroprocessing: transition metal phosphides. *J. Catal.* **2003**, *216*, 343−352.
(41) Alvarado Rupflin, L.; Mormul, J.; Lejkowski, M.; Titlbach, S.; Papp, R.; Gläser, R.; Dimitrakopoulou, M.; Huang, X.; Trunschke, A.; Willinger, M. G.; Schlögl, R.; Rosowski, F.; Schunk, S. A. Platinum Group Metal Phosphides as Heterogeneous Catalysts for the Gas-Phase Hydroformylation of Small Olefins. *ACS Catal.* **2017**, *7*, 3584−3590.
(42) Ko, J.; Muhlenkamp, J. A.; Bonita, Y.; LiBretto, N. J.; Miller, J. T.; Hicks, J. C.; Schneider, W. F. Experimental and Computational Investigation of the Role of P in Moderating Ethane Dehydrogenation Performance over Ni-Based Catalysts. *Ind. Eng. Chem. Res.* **2020**, *59*, 12666−12676.
(43) Yao, Y.; Zuo, M.; Zhou, H.; Li, J.; Shao, H.; Jiang, T.; Liao, X.; Lu, S. One-Pot Preparation of Ni_2P/γ-Al_2O_3 Catalyst for Dehydrogenation of Propane to Propylene. *ChemistrySelect* **2018**, *3*, 10532−10536.
(44) Zhu, Q.; Zhang, H.; Zhang, S.; Wang, G.; Zhu, X.; Li, C. Dehydrogenation of Isobutane over a Ni−P/SiO_2 Catalyst: Effect of P Addition. *Ind. Eng. Chem. Res.* **2019**, *58*, 7834−7843.

(45) Li, J.; Chai, Y.; Liu, B.; Wu, Y.; Li, X.; Tang, Z.; Liu, Y.; Liu, C. The catalytic performance of Ni_2P/Al_2O_3 catalyst in comparison with Ni/Al_2O_3 catalyst in dehydrogenation of cyclohexane. *Appl. Catal., A* **2014**, *469*, 434−441.

(46) Xu, Y.; Wang, X.; Lv, R. Interaction between Cs and Ni_2P/SiO_2 for enhancing isobutane dehydrogenation in the presence of hydrogen. *React. Kinet. Mech. Catal.* **2014**, *113*, 393−406.

(47) Ma, R.; Yang, T.; Gao, J.; Kou, J.; Chen, J. Z.; He, Y.; Miller, J. T.; Li, D. Composition tuning of Ru-based phosphide for enhanced propane selective dehydrogenation. *ACS Catal.* **2020**, *10*, 10243−10252.

(48) Ravel, B.; Newville, M. Athena, artemis, hephaestus: data analysis for X-ray absorption spectroscopy using IFEFFIT. *J. Synchrotron Radiat.* **2005**, *12*, 537−541.

(49) Hammersley, A. P.; Svensson, S. O.; Hanfland, M.; Fitch, A. N.; Hausermann, D. Two-dimensional detector software: from real detector to idealised image or two-theta scan. *High Pres. Res.* **1996**, *14*, 235−248.

(50) Lutterotti, L.; Matthies, S.; Wenk, H.-R.; Schultz, A. S.; Richardson, J. W., Jr. Combined texture and structure analysis of deformed limestone from time-of-flight neutron diffraction spectra. *J. Appl. Phys.* **1997**, *81*, 594−600.

(51) Bolin, T. B.; Wu, T.; Schweitzer, N.; Lobo-Lapidus, R.; Kropf, A. J.; Wang, H.; Hu, Y.; Miller, J. T.; Heald, S. M. *In situ* intermediate-energy X-ray catalysis research at the advanced photon source beamline 9-BM. *Catal. Today* **2013**, *205*, 141−147.

(52) Read, C. G.; Callejas, J. F.; Holder, C. F.; Schaak, R. E. General strategy for the synthesis of transition metal phosphide films for electrocatalytic hydrogen and oxygen evolution. *ACS Appl. Mater. Interfaces* **2016**, *8*, 12798−12803.

(53) Popczun, E. J.; McKone, J. R.; Read, C. G.; Biacchi, A. J.; Wiltrout, A. M.; Lewis, N. S.; Schaak, R. E. Nanostructured nickel phosphide as an electrocatalyst for the hydrogen evolution reaction. *J. Am. Chem. Soc.* **2013**, *135*, 9267−9270.

(54) Li, J.; Li, J.; Zhou, X.; Xia, Z.; Gao, W.; Ma, Y.; Qu, Y. Highly efficient and robust nickel phosphides as bifunctional electrocatalysts for overall water-splitting. *ACS Appl. Mater. Interfaces* **2016**, *8*, 10826−10834.

(55) Miller, J.; Schreier, M.; Kropf, A. J.; Regalbuto, J. R. A fundamental study of platinum tetraammine impregnation of silica: 2. The effect of method of preparation, loading, and calcination temperature on (reduced) particle size. *J. Catal.* **2004**, *225*, 203−212.

(56) Miller, J. T.; Kropf, A. J.; Zha, Y.; Regalbuto, J. R.; Delannoy, L.; Louis, C.; Bus, E.; van Bokhoven, J. A. The effect of gold particle size on AuAu bond length and reactivity toward oxygen in supported catalysts. *J. Catal.* **2006**, *240*, 222−234.

(57) Wu, Z.; Bukowski, B. C.; Li, Z.; Milligan, C.; Zhou, L.; Ma, T.; Wu, Y.; Ren, Y.; Ribeiro, F. H.; Delgass, W. N.; Greeley, J.; Zhang, G.; Miller, J. T. Changes in catalytic and adsorptive properties of 2 nm Pt_3Mn nanoparticles by subsurface atoms. *J. Am. Chem. Soc.* **2018**, *140*, 14870−14877.

(58) Fung, S. XPS studies of strong metal-support interactions (SMSI)-Pt/TiO_2. *J. Catal.* **1982**, *76*, 225−230.

(59) Dake, L. S.; Baer, D. R.; Friedrich, D. M. Auger parameter measurements of phosphorus compounds for characterization of phosphazenes. *J. Vac. Sci. Technol. A* **1989**, *7*, 1634−1638.

(60) Pryadchenko, V. V.; Srabionyan, V. V.; Avakyan, L. A.; van Bokhoven, J. A.; Bugaev, L. A. Electronic Structure of Pt and Au Compounds Measured by X-ray Emission and X-ray Absorption Spectroscopies. *J. Phys. Chem. C* **2012**, *116*, 25790−25796.

(61) Purdy, S. C.; Ghanekar, P.; Mitchell, G.; Kropf, A. J.; Zemlyanov, D. Y.; Ren, Y.; Ribeiro, F.; Delgass, W. N.; Greeley, J.; Miller, J. T. Origin of electronic modification of platinum in a Pt_3V alloy and their consequences for propane dehydrogenation catalysis. *ACS Appl. Energy Mater.* **2020**, *3*, 1410−1422.

(62) Hu, B.; "Bean" Getsoian, A.; Schweitzer, N. M.; Das, U.; Kim, H.; Niklas, J.; Poluektov, O.; Curtiss, L. A.; Stair, P. C.; Miller, J. T.; Hock, A. S. Selective propane dehydrogenation with single-site CoII on SiO_2 by a non-redox mechanism. *J. Catal.* **2015**, *322*, 24−37.

(63) Schweitzer, N. M.; Hu, B.; Das, U.; Kim, H.; Greeley, J.; Curtiss, L. A.; Stair, P. C.; Miller, J. T.; Hock, A. S. Propylene hydrogenation and propane dehydrogenation by a single-site Zn^{2+} on silica catalyst. *ACS Catal.* **2014**, *4*, 1091−1098.

(64) Cybulskis, V. J.; Pradhan, S. U.; Lovón-Quintana, J. J.; Hock, A. S.; Hu, B.; Zhang, G.; Delgass, W. N.; Ribeiro, F. H.; Miller, J. T. The Nature of the Isolated Gallium Active Center for Propane Dehydrogenation on Ga/SiO_2. *Catal. Lett.* **2017**, *147*, 1252−1262.

(65) Hu, C.; Shao, M.; Xiang, M.; Li, S.; Xu, S. The role of hydrogen coverage and location in 1,3-butadiene hydrogenation over Pt/SiO_2. *React. Chem. Eng.* **2020**, *5*, 87−100.

(66) Jugnet, Y.; Sedrati, R.; Bertolini, J. Selective hydrogenation of 1,3-butadiene on Pt 3Sn(111) alloys: comparison to Pt(111). *J. Catal.* **2005**, *229*, 252−258.

(67) Searles, K.; Siddiqi, G.; Safonova, O. V.; Copéret, C. Silica-supported isolated gallium sites as highly active, selective and stable propane dehydrogenation catalysts. *Chem. Sci.* **2017**, *8*, 2661−2666.

(68) Xu, Y.; Sang, H.; Wang, K.; Wang, X. Catalytic dehydrogenation of isobutane in the presence of hydrogen over Cs-modified Ni_2P supported on active carbon. *Appl. Surf. Sci.* **2014**, *316*, 163−170.

(69) Bond, G. C.; Dowden, D. A.; Mackenzie, N. The selective hydrogenation of acetylene. *Trans. Faraday Soc.* **1958**, *54*, 1537−1546.

(70) Than, C. N.; Didillon, B.; Sarrazin, P.; Cameron, C. Catalytic hydrogenation process and a catalyst for use in the process. U.S. Patent 5,648,576 A, 1999.

(71) George, P. P.; Gedanken, A.; Gabashvili, A. Synthesis of stable spherical platinum diphosphide, PtP_2/carbon nanocomposite by reacting Pt $(PPh_3)_4$ at elevated temperature under autogenic pressure. *Mater. Res. Bull.* **2007**, *42*, 626−632.

(72) Coleman, N., Jr.; Lovander, M. D.; Leddy, J.; Gillan, E. G. Phosphorus-rich metal phosphides: direct and tin flux-assisted synthesis and evaluation as hydrogen evolution electrocatalysts. *Inorg. Chem.* **2019**, *58*, 5013−5024.

(73) Jiang, J.; Wang, C.; Zhang, J.; Wang, W.; Zhou, X.; Pan, B.; Tang, K.; Zuo, J.; Yang, Q. Synthesis of FeP_2/C nanohybrids and their performance for hydrogen evolution reaction. *J. Mater. Chem. A* **2015**, *3*, 499−503.

(74) Prins, R. Hydrogen spillover. Facts and fiction. *Chem. Rev.* **2012**, *112*, 2714−2738.

(75) Li, X.; Zhou, J.; Huang, J.; Bu, T.; Ma, Y. Advances of Pt catalysts for propane catalytic dehydrogenation to propylene. *Pet. Process. Petrochem.* **2019**, *50*, 102−108.

(76) Otroshchenko, T.; Jiang, G.; Kondratenko, V. A.; Rodemerck, U.; Kondratenko, E. V. Current status and perspectives in oxidative, non-oxidative and CO_2-mediated dehydrogenation of propane and isobutane over metal oxide catalysts. *Chem. Soc. Rev.* **2021**, *50*, 473−527.

(77) Docherty, S. R.; Rochlitz, L.; Payard, P.-A.; Copéret, C. Heterogeneous alkane dehydrogenation catalysts investigated via a surface organometallic chemistry approach. *Chem. Soc. Rev.* **2021**, *50*, 5806−5822.

(78) Han, S.; Zhao, D.; Otroshchenko, T.; Lund, H.; Bentrup, U.; Kondratenko, V. A.; Rockstroh, N.; Bartling, S.; Doronkin, D. E.; Grunwaldt, J.-D.; Rodemerck, U.; Linke, D.; Gao, M.; Jiang, G.; Kondratenko, E. V. Elucidating the Nature of Active Sites and Fundamentals for their Creation in Zn-Containing ZrO_2−Based Catalysts for Nonoxidative Propane Dehydrogenation. *ACS Catal.* **2020**, *10*, 8933−8949.

(79) Hu, B.; Schweitzer, N. M.; Zhang, G.; Kraft, S. J.; Childers, D. J.; Lanci, M. P.; Miller, J. T.; Hock, A. S. Isolated FeII on silica as a selective propane dehydrogenation catalyst. *ACS Catal.* **2015**, *5*, 3494−3503.

(80) Zhang, H.; Liu, G.; Shi, L.; Ye, J. Single-atom catalysts: emerging multifunctional materials in heterogeneous catalysis. *Adv. Energy Mater.* **2018**, *8*, 1701343.

(81) Yang, X.-F.; Wang, A.; Qiao, B.; Li, J.; Liu, J.; Zhang, T. Single-Atom Catalysts: A New Frontier in Heterogeneous Catalysis. *Acc. Chem. Res.* **2013**, *46*, 1740.

https://doi.org/10.1021/acscatal.1c03970
ACS Catal. 2021, 11, 13496−13509

(82) Sharma, P.; Kumar, S.; Tomanec, O.; Petr, M.; Zhu Chen, J.; Miller, J. T.; Varma, R. S.; Gawande, M. B.; Zbořil, R. Carbon nitride-based ruthenium single atom photocatalyst for CO_2 reduction to methanol. *Small* **2021**, *17*, 2006478.
(83) Kadam, R. G.; Zhang, T.; Zaoralová, D.; Medved, M.; Bakandritsos, A.; Tomanec, O.; Petr, M.; Zhu Chen, J.; Miller, J. T.; Otyepka, M.; Zboril, R.; Asefa, T.; Gawande, M. B. Single Co-atoms as electrocatalysts for efficient hydrazine oxidation reaction. *Small* **2021**, *17*, 2006477.
(84) Marshall-Roth, T.; Libretto, N. J.; Wrobel, A. T.; Anderton, K.; Surendranath, Y. A Pyridinic Fe-N4 macrocycle effectively models the active sites in Fe/N-doped carbon electrocatalysts. *Nat. Commun.* **2019**, *11*, 5283.

https://doi.org/10.1021/acscatal.1c03970
ACS Catal. 2021, 11, 13496−13509